to be restricted particularly in chest CT owing to concomitant degradation of spatial resolution, since image sharpness is critical for interpretation of the lung [3].

The iterative reconstruction technique, which has recently become available on commercial CT scanners, enables noise reduction with essentially no trade-off in spatial resolution [4]. Previous studies for chest CT showed that iterative reconstruction helped reduce the radiation dose and improve image quality by reducing noise compared with the conventional FBP technique [5–8]. Iterative reconstruction, however, is not free from unfavorable effects. Use of it alters the texture of image noise and can yield a unusually homogenous image, which may not be immediately appealing to most radiologists usually accustomed to the FBP image [9]. It is also known that an excessive degree of iterative reconstruction may obscure fine and subtle findings [7].

In this study, we focused on subjective assessment of image quality using a method based on Anderson's functional measurement theory. The theory was originally developed for description of non-observable psychological processes and has been applied efficiently to image quality assessment [10–12]. With this method, the subjective image quality can be represented as a score on an interval scale, facilitating comparison of quality of images obtained with different parameters.

The aims of this study were to assess the effect of iterative reconstruction on the quality of lung CT images in relation to radiation dose and to investigate attainable degree of dose reduction compared with FBP.

Materials and methods

Image acquisition

One pair of porcine lungs inflated and fixed with Heitzman's method [13] placed in an oval polymethylmethacrylate phantom with a long axis of 33.3 cm and a short axis of 23.1 cm was scanned with a 64-slice CT system (Discovery CT 750HD; GE Healthcare, Milwaukee, WI). Since the lungs used are small (about 11 cm in the longest diameter) and have no other extra-thoracic soft tissue except for the thoracic vertebra and rib cage, a smaller radiation dose was likely to be sufficient compared with standard dose for human lungs. Therefore, we assumed a standard dose for the porcine lungs using automatic exposure control of the scanner (AutomA; GE Healthcare) to keep the noise level similar to routine clinical lung CT. Using AutomA, a tube current time product of 40 mAs was chosen as standard, with a noise index of 11 for a 5-mm-thick image and a standard reconstruction kernel. A half dose and a quarter dose of the standard (i.e., 20 and 10 mAs) were also used for reduced-dose mode, and a 400-mAs dose was used to create high-quality images. Helical scans were performed with scanning parameters including a tube voltage of 120 kVp, a detector configuration of 64 × 0.625 mm and a beam pitch of 0.984:1. Image data were reconstructed with an FBP algorithm with a standard kernel into 5-mm-thick axial images with 512 × 512 pixels and a 350-mm field of view. The data obtained at 10, 20 and 40 mAs were also reconstructed with ASIR, an implementation of iterative reconstruction techniques (Table 1). In reconstruction with ASIR, the original FBP and the fully converged ASIR (100%-ASIR) images are blended to give the final ASIR image. Although increasing the ratio of the full ASIR data to the FBP data results in reduction of image noise, it also changes the texture of noise and may cause loss of diagnostic information. Because of the paucity of available data about appropriate blending ratio of ASIR for chest CT at the time of the experiment, we chose blending ratios of 20 and 40% according to the result of a previous study [9].

Using picture archiving and communication system equipment (Centricity; GE Healthcare, Milwaukee, WI) with a DICOM-compliant 21-inch 2-megapixel liquid crystal display (LCD) monitor (Radiforce R22; Eizo Nanao, Ishikawa, Japan), one of the authors with 11 years' experience in reading lung CT images selected a slice without major artifacts from the image set obtained at 400 mAs. This image was saved into a TIFF format file with a fixed lung window setting (window width and level were 600 and −900, respectively). The window was determined so that CT images of the fixed porcine lungs resembled typical human lung CT images in terms of subjective image noise and visually reproduction of lung structures. Images at the same slice level with different doses or reconstruction methods were saved in a similar

Table 1 Doses and algorithms used for image acquisition and reconstruction

Image	Dose (mAs)	Reconstruction
A_0	10	FBP
A_{20}	10	20%-ASIR
A_{40}	10	40%-ASIR
B_0	20	FBP
B_{20}	20	20%-ASIR
B_{40}	20	40%-ASIR
C_0	40	FBP
C_{20}	40	20%-ASIR
C_{40}	40	40%-ASIR
D_0	400	FBP

FBP filtered back projection, *ASIR* adaptive statistical iterative reconstruction

manner. Images were then cropped to 256 × 256 pixels by trimming a peripheral portion out of the thoracic cage with ImageJ software (ImageJ, version 1.42; National Institutes of Health, Bethesda, MD). The ten resulting images were evaluated in the current study (Fig. 1).

Qualitative analysis

One trained and two board-certified radiologists with 4, 7 and 7 years' experience in reading chest CT images independently evaluated the quality of each image in the following three areas: noise of lung parenchyma, image sharpness and conspicuity of tiny nodules. For evaluating image sharpness, readers were asked to evaluate the sharpness of the walls of the bronchovascular structures and the extent to which the peripheries of the structures were visible. Nodules were about 1 mm in diameter and predominantly seen in peripheral areas of the lungs, indicating probable calcified granulomas. Experiments were performed based on Anderson's functional measurement theory [10, 11, 14]. It was originally developed in the area of psychology and has been applied efficiently to image quality assessment [10–12]. Experiments using the theory involve three steps: showing images as a pair, rating the perceived difference in image quality and calculating subjective quality scores (SQSs). To display images and

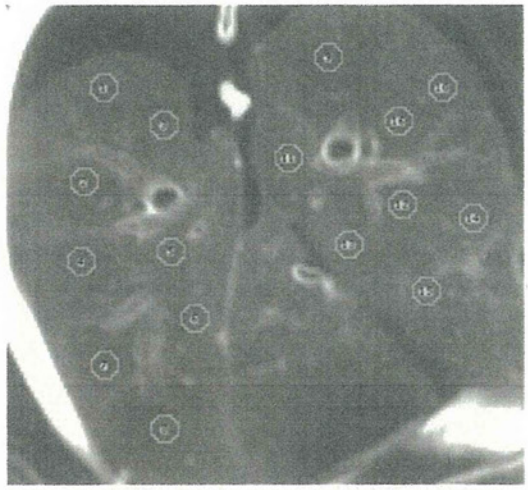

Fig. 2 16 circular regions of interest (ROIs) with a size of 24.3 mm^2 are placed on lung parenchyma, avoiding apparent structures and major artifacts. The 16 measurements for each image were averaged. To measure at the same positions, ROIs were copied between images

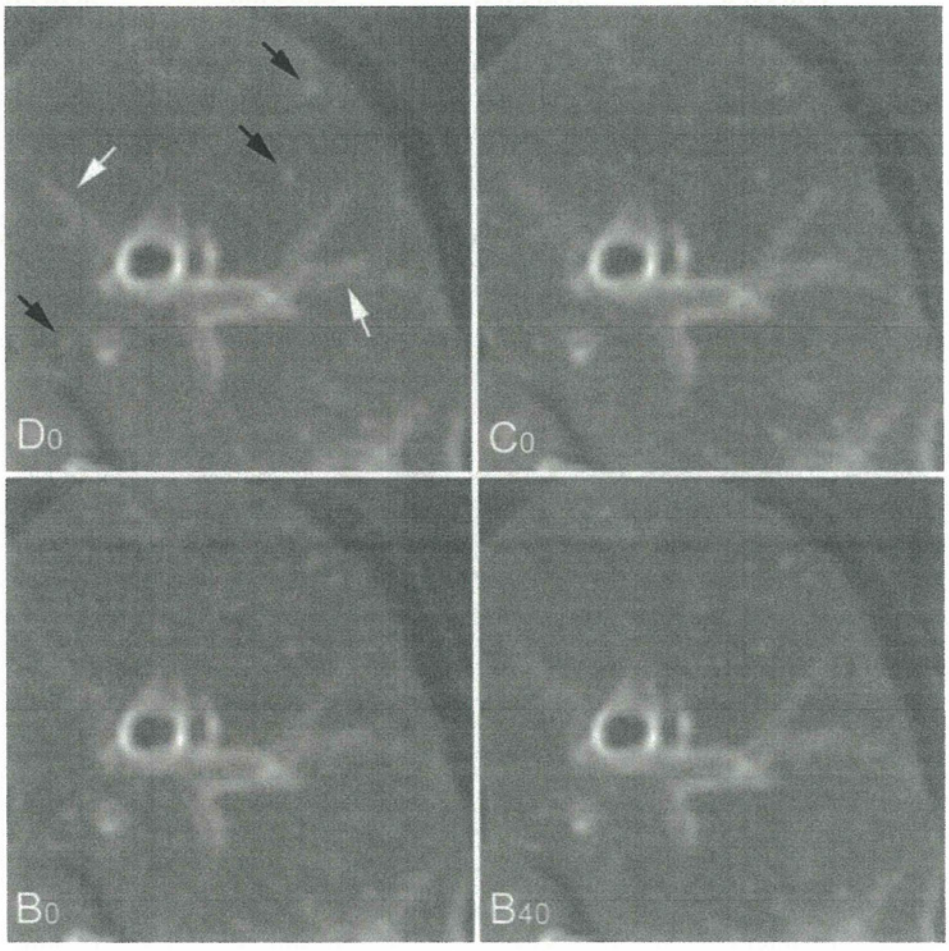

Fig. 1 *Upper left* image D_0, *upper right* image C_0, *lower left* image B_0, *lower right* image B_{40}. *Black arrows* in image D_0 indicate tiny nodules and *white arrows* bronchovascular structures. Compared with image C_0, image B_0, which was obtained at a half dose, appears noisy, and bronchovascular structures and nodules on image B_0 are blurred. The subjective quality scores (SQSs) for image B_0 were significantly lower than those for image C_0 for noise (−0.41 vs. 0.47, $P < 0.001$) and for sharpness (−0.18 vs. 0.64, $P = 0.015$). From comparison between image B_0 and image B_{40}, image quality apparently improved with 40% ASIR. The SQSs for image B_{40} were comparable to those for image C_0 on noise (0.43 vs. 0.47, $P > 0.999$). Although no statistically significant results were observed, sharpness was worse on B_{40} than on C_0 (0.43 vs. 0.64, $P = 0.985$), and conspicuity of nodules was better on B_{40} than on C_0 (0.70 vs. 0.37, $P = 0.551$)

record the reader's rating, an in-house program written in JAVA language running on the PACS system was used. One hundred image pairs, generated by a factorial combination of the ten prepared images, were presented on the LCD monitor in random order. Readers rated differences in quality between adjacently displayed paired images from −10 to 10, using a slider displayed below the images, without time limits or knowledge of parameters for image acquisition. The sign of the scores indicated the side of the preferred image. For each evaluation area, presenting image pairs twice and averaging the scores of two sessions yielded a 10 × 10 matrix with elements of scores, where the row and column of the matrix corresponded to the images displayed on the right and left sides. To minimize the interindividual variation caused by the range used in rating, elements of the data matrix were normalized using the z score transformation [10, 11]. The z score z for a score s is given by $z = (s - \mu)/\sigma$, where μ and σ are the mean and standard deviation of scores. Before the calculation based on the Anderson's functional measurement theory, it is required to observe parallelism for data within the different rows and columns of the matrix graphically or to calculate the interaction between rows and columns by means of two-way analysis of variance method (ANOVA) [10, 11]. Then the SQS for image i, SQS_i, can be calculated from the data matrix as follows, according to the theory,

$$SQS_i = \frac{\overline{r}_{i\bullet} - \overline{r}_{\bullet i}}{2}.$$

Here $\overline{r}_{i\bullet}$ represents the marginal mean for row i of the matrix, and $\overline{r}_{\bullet i}$ represents the marginal mean for column i of the matrix. Before an actual test session, readers practiced for several minutes with an image set consisting of images at the 1 cm caudal level, in order to become

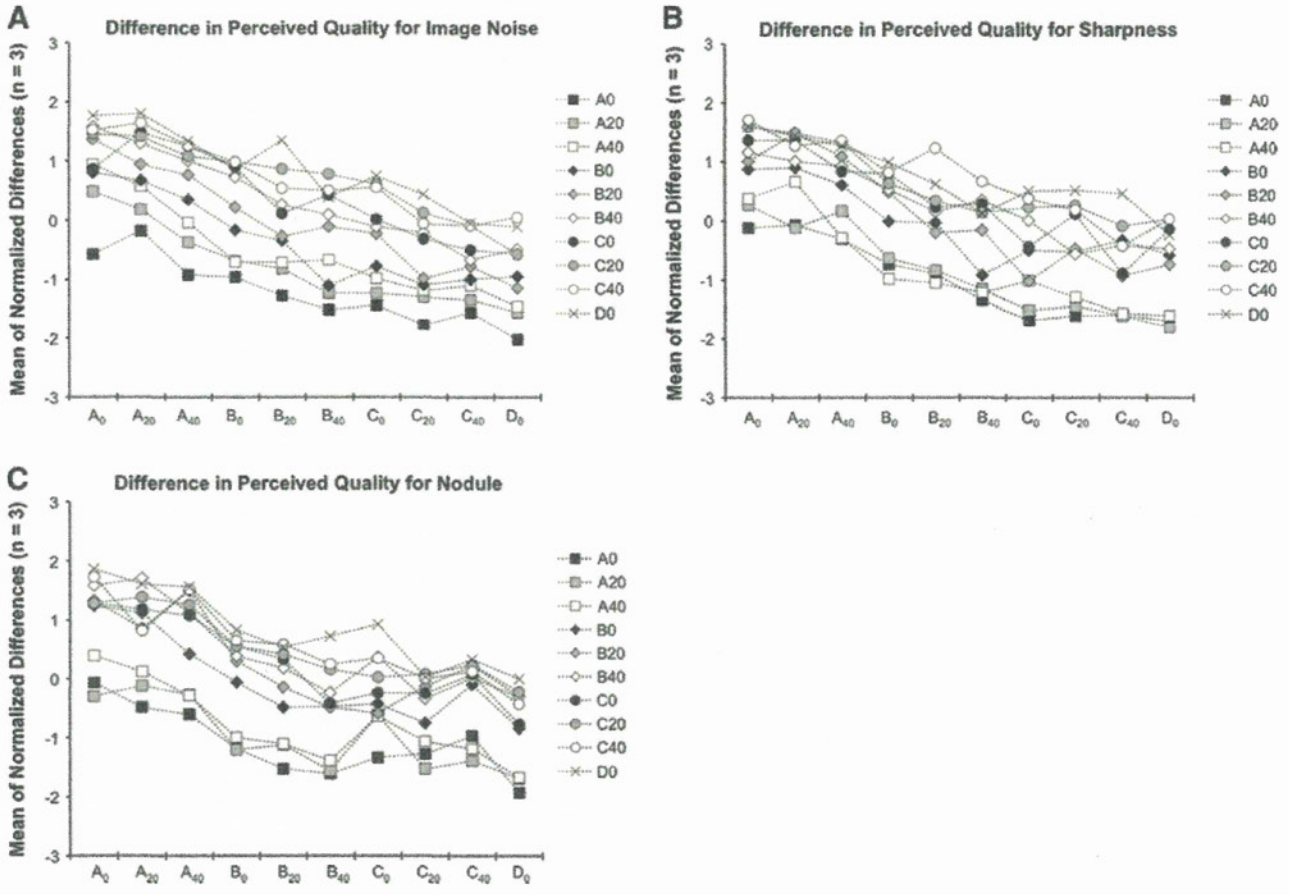

Fig. 3 Result of experiments for qualitative analysis of image noise, averaged for all readers. Each curve corresponds to images displayed on the right side of the monitor, and the label on the x axis indicates images on the left side. Points on curves correspond to perceived difference in quality between paired images. Before averaging between readers, individual scores were normalized using the z score transformation. Note the approximate parallelism of the data. Similar parallelisms were also observed on both image sharpness and conspicuity of tiny nodules. To observe parallelism of data graphically or, more preferably, to confirm no interaction between the rows and columns of data matrix by means of two-way analysis of variance method (ANOVA) is necessary for calculation for the subjective quality score for each image based on Anderson's functional measurement theory. Result of two-way ANOVA showed no significant interactions between rows and columns of the data ($P = 0.248$ for noise, $P = 0.717$ for sharpness and $P = 0.867$ for nodules)

familiar with the method of evaluation and the range of image quality.

To minimize the increased risk of type I errors due to multiple testing, SQSs were analyzed by Tukey's honestly significant differences test using a statistical suite (R, version 2.9.2; http://www.R-project.org, R Foundation for Statistical Computing, Vienna, Austria).

Quantitative analysis

An experienced radiologist measured the standard deviation of attenuation values (image SD) as quantitative noise data with ImageJ by placing 16 circular regions of interest (ROIs) with a size of 24.3 mm^2 on lung parenchyma, avoiding apparent structures and major artifacts (Fig. 2). The 16 measurements for each image were averaged. To measure at the same positions, ROIs were copied between images. Pearson's correlation coefficients between image SDs and SQSs were calculated.

Results

Figure 3 shows approximate parallelism of data in the rating of experiments for image noise. After no significant row-column interaction was confirmed using two-way ANOVA tests ($P = 0.248$ for noise, $P = 0.717$ for sharpness and $P = 0.867$ for nodules), SQSs were calculated (Tables 2, 3, 4).

As expected, the objective noise of the FBP image decreased as the dose increased (Fig. 4). At 10–40 mAs,

Table 2 Subjective quality scores for noise

Image	SQS (mean ± SD)	Comparison by Tukey's HSD									
		A_0	A_{20}	A_{40}	B_0	B_{20}	B_{40}	C_0	C_{20}	C_{40}	D_0
A_0	−1.12 ± 0.10	–									
A_{20}	−0.88 ± 0.08	NS	–								
A_{40}	−0.55 ± 0.13	**	**	–							
B_0	−0.29 ± 0.07	**	**	*	–						
B_{20}	0.00 ± 0.10	**	**	**	*	–					
B_{40}	0.30 ± 0.06	**	**	**	**	*	–				
C_0	0.33 ± 0.03	**	**	**	**	**	NS	–			
C_{20}	0.65 ± 0.04	**	**	**	**	**	**	**	–		
C_{40}	0.70 ± 0.09	**	**	**	**	**	**	**	NS	–	
D_0	0.87 ± 0.12	**	**	**	**	**	**	**	NS	NS	–

Image labels are defined in Table 1

SQS subjective quality score, *SD* standard deviation, *Tukey's HSD* Tukey's honestly significant differences test

NS $P \geq 0.05$, * $P < 0.05$, ** $P < 0.01$

Table 3 Subjective quality scores for sharpness

Image	SQS (mean ± SD)	Comparison by Tukey's HSD									
		A_0	A_{20}	A_{40}	B_0	B_{20}	B_{40}	C_0	C_{20}	C_{40}	D_0
A_0	−0.99 ± 0.23	–									
A_{20}	−0.90 ± 0.08	NS	–								
A_{40}	−0.75 ± 0.05	NS	NS	–							
B_0	−0.12 ± 0.29	**	**	**	–						
B_{20}	0.05 ± 0.15	**	**	**	NS	–					
B_{40}	0.30 ± 0.09	**	**	**	NS	NS	–				
C_0	0.43 ± 0.09	**	**	**	*	NS	NS	–			
C_{20}	0.54 ± 0.07	**	**	**	**	NS	NS	NS	–		
C_{40}	0.73 ± 0.20	**	**	**	**	**	NS	NS	NS	–	
D_0	0.72 ± 0.26	**	**	**	**	**	NS	NS	NS	NS	–

Image labels are defined in Table 1

SQS subjective quality score, *SD* standard deviation, *Tukey's HSD* Tukey's honestly significant differences test

NS $P \geq 0.05$, * $P < 0.05$, ** $P < 0.01$

Table 4 Subjective quality scores for nodules

Image	SQS (mean ± SD)	Comparison by Tukey's HSD									
		A_0	A_{20}	A_{40}	B_0	B_{20}	B_{40}	C_0	C_{20}	C_{40}	D_0
A_0	−1.07 ± 0.12	–									
A_{20}	−0.90 ± 0.14	NS	–								
A_{40}	−0.76 ± 0.12	NS	NS	–							
B_0	−0.01 ± 0.09	**	**	**	–						
B_{20}	0.25 ± 0.10	**	**	**	NS	–					
B_{40}	0.48 ± 0.01	**	**	**	*	NS	–				
C_0	0.25 ± 0.14	**	**	**	NS	NS	NS	–			
C_{20}	0.52 ± 0.06	**	**	**	**	NS	NS	NS	–		
C_{40}	0.41 ± 0.34	**	**	**	*	NS	NS	NS	NS	–	
D_0	0.83 ± 0.01	**	**	**	**	**	NS	**	NS	*	–

Image labels are defined in Table 1

SQS subjective quality score, *SD* standard deviation, *Tukey's HSD* Tukey's honestly significant differences test

NS $P \geq 0.05$, * $P < 0.05$, ** $P < 0.01$

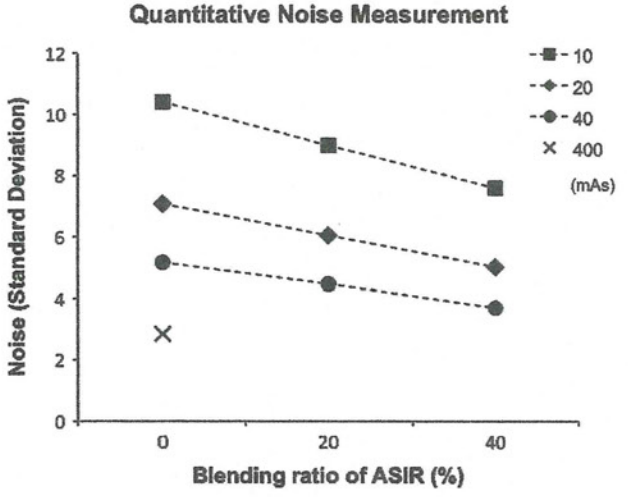

Fig. 4 Objective image noise measured as the standard deviation of attenuation values is plotted against blending ratio of ASIR. As expected, objective noise of 0%-ASIR image (FBP image) decreases as dose increases. At 10–40 mAs, image noise decreases almost linearly as the percentage of ASIR increases

objective noise decreased almost linearly as the percentage of ASIR increased, which is consistent with the result of a previous study [9].

SQSs are plotted against quantitative noise data in Fig. 5. In general, both SQS and image SD were improved with increasing the scan dose and the blending ratio of ASIR. The correlation between the mean SQS and image SD was good (Pearson's correlation coefficient: $r = -0.991$ for noise, −0.967 for sharpness and −0.953 for nodule, respectively).

At all doses, applying 40% ASIR to an FBP image increased the SQS for noise significantly ($P < 0.01$, at all doses). Applying 40% ASIR to an FBP image also increased the SQSs for image sharpness and conspicuity of tiny nodules, but these increases were generally not significant. A half dose 40%-ASIR image (B_{40}) had a slightly smaller SD value than the standard dose FBP image (C_0) (5.0 vs. 5.2) and was comparable in terms of SQSs (0.30 vs. 0.33, $P = 1.000$ for noise; 0.30 vs. 0.43, $P = 0.993$ for sharpness; 0.48 vs. 0.25, $P = 0.653$ for nodules). A quarter dose 40%-ASIR image (A_{40}) had a slightly higher SD value than the half dose FBP image (B_0) (7.6 vs. 7.1) and was significantly worse than the image B_0 in terms of SQSs (−0.55 vs. −0.29, $P = 0.038$ for noise; −0.75 vs. −0.12, $P = 0.007$ for sharpness; −0.76 vs. −0.01, $P < 0.001$ for nodules).

Discussion

On assessment of image quality, objective analysis is considered to be superior to subjective analysis in terms of accuracy and reproducibility of the result and suitable for strict quality assessment of technologies or products. For quality check of clinical images, however, assessment by the expert in medical imaging is still necessary at the present time because no objective measurements give a precise enough prediction of perceived image quality for the expert to abandon the subjective analysis. In the present study, a method based on Anderson's functional measurement theory was applied for the subjective analysis. Presenting images as a pair, by placing images side by side or toggling between two images by user operation [15], helps readers to evaluate the superiority or inferiority of images in more detail than presenting images separately. Presentation of image pairs is also utilized in the double-stimulus continuous-quality scale (DSCQS) method, which is a

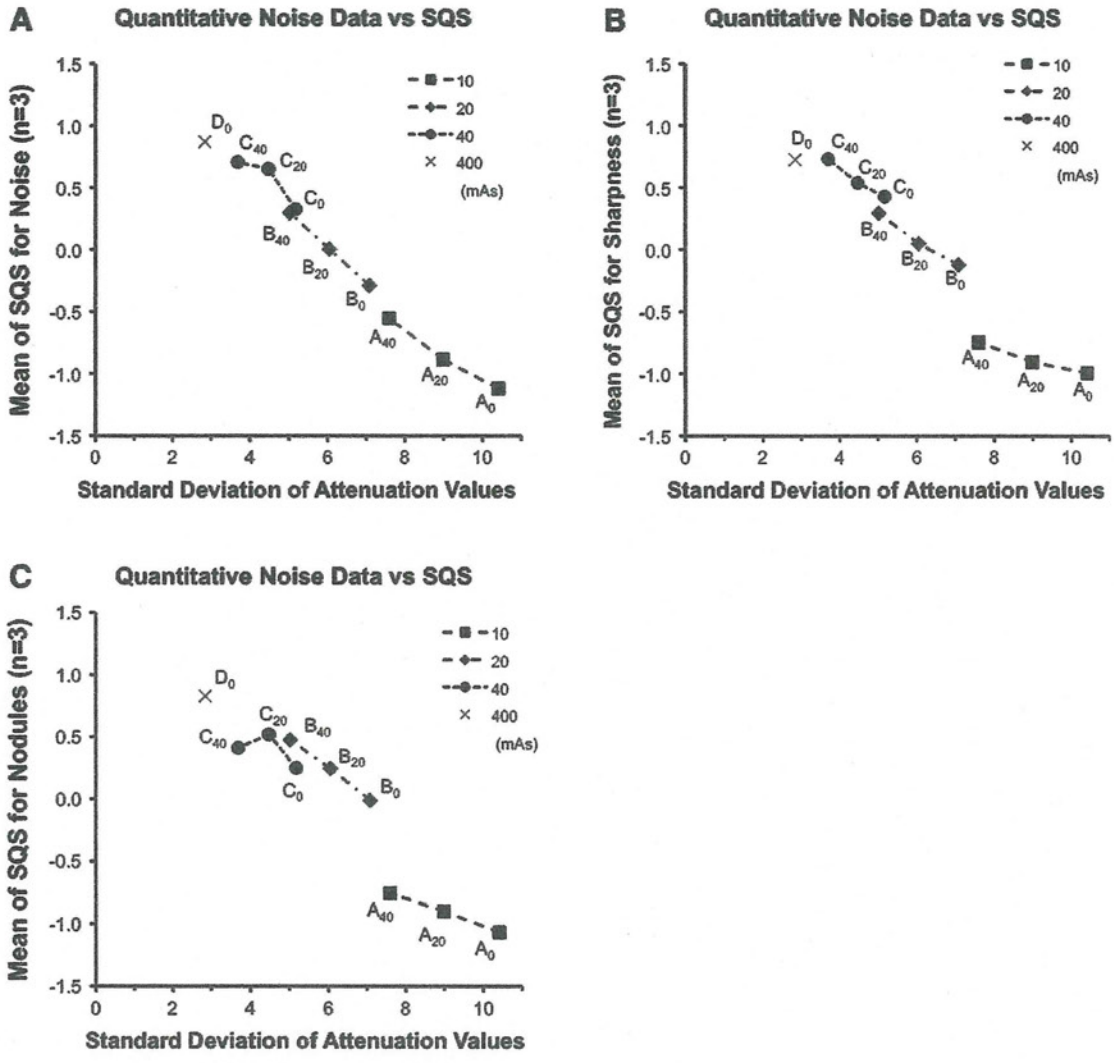

Fig. 5 The mean of the subjective quality score (*SQS*) is plotted against the standard deviation of attenuation (image SD). The correlation between the mean of SQS and the image SD is relatively good (Pearson's coefficient of correlation: $r = -0.991$ for noise, -0.967 for sharpness, and -0.953 for nodules). Image A_{40} had a higher SD value than image B_0 (7.6 vs. 7.1, respectively) and significantly lower SQSs than image B_0 (-0.55 vs. -0.29, $P = 0.038$ for noise; -0.75 vs. -0.12, $P = 0.007$ for sharpness and -0.76 vs. -0.01, $P < 0.001$ for nodules, respectively). **a** Noise, **b** sharpness, **c** nodules

popular method for assessment of image quality in the field of broadcasting proposed by the International Telecommunication Union. Use of a scale with at least ten steps is recommended by functional measurement theory [14]. A psychological study reported that, irrespective of popular use, a five-point scale was not optimal and more response categories appeared better with regard to reliability, validity and discriminating power [16]. We think the method in the present study was likely to evaluate superiority and inferiority of image quality more sensitively and reliably than conventional five-step rating.

In the present study, a 40%-ASIR image obtained at half dose generally had comparable image quality to the standard-dose FBP image. The 40%-ASIR images obtained at the quarter dose were worse than half-dose FBP images with regard to both the image SD and subjective score. According to the trend seen in Fig. 3, it may be difficult to improve subjective image quality of the quarter dose image to the level of the half-dose FBP image. These results may imply that using ASIR cannot compensate for the degradation of quality of a reduced-dose image at a lower range of scan doses as well as at a standard range. If a low-dose scan protocol for clinical lung imaging had already been used, considerable dose reduction would not have been achievable using ASIR.

In the present study, fairly good linear correlation was observed between the subjective score and the objective measurement for image noise. Although ASIR changes

noise texture [4, 6], the change had less effect on the perceived amount of image noise. Relatively good correlation was also observed between the SQS and the image SD with regard to sharpness and visualization of tiny nodules. The image SD may be used as a rough predictor of subjective image quality as long as the dose reduction is less than 50%.

This study had limitations. Since no human images were assessed, results of this study may not directly apply to clinical imaging. The assumed standard dose for porcine lungs may not simulate a standard dose of clinical lung imaging as well. Use of a slice thickness of 5 mm is another major limitation of this study. Smaller slice thicknesses are currently used in clinical chest imaging, and many normal and abnormal findings on chest CT are visualized suboptimally on 5-mm slices. This may significantly affect the result particularly for the evaluation of approximately 1-mm peripheral nodules. Another limitation is that a reconstruction kernel that emphasizes a high frequency component was not used. With such a kernel, image noise would increase, and use of ASIR might be more effective. Experiments with a thinner slice and a kernel emphasizing high frequency would be more suitable for considering the quality of ASIR images for lung CT. Lesions with ground-glass opacity including bronchioloalveolar carcinoma and interstitial pneumonia were not evaluated, nor were low attenuating areas present in emphysema. Images with an ASIR level of more than 40% were not evaluated. A higher degree of ASIR would be beneficial for dose reduction in some clinical situations like screening. A recent article using clinical images reported that images reconstructed with a higher percentage of ASIR (70%) had a blothy pixilated texture, which did not affect the diagnostic confidence [17]. Application of Anderson's functional measurement theory in medical research is not common, and the reproducibility of the result was not tested.

In conclusion, compared to the FBP algorithm, ASIR for lung CT may enable an approximately 50% reduction in dose from the standard dose, and visualization of small structures is preserved.

Acknowledgments None.

References

1. Mettler FA Jr, Bhargavan M, Faulkner K, Gilley DB, Gray JE, Ibbott GS, et al. Radiologic and nuclear medicine studies in the United States and worldwide: frequency, radiation dose, and comparison with other radiation sources—1950–2007. Radiology. 2009;253:520–31.
2. Berrington de Gonzalez A, Darby S. Risk of cancer from diagnostic X-rays: estimates for the UK and 14 other countries. Lancet. 2004;363:345–51.
3. Kubo T, Lin PJ, Stiller W, Takahashi M, Kauczor HU, Ohno Y, et al. Radiation dose reduction in chest CT: a review. AJR Am J Roentgenol. 2008;190:335–43.
4. Marin D, Nelson RC, Schindera ST, Richard S, Youngblood RS, Yoshizumi TT, et al. Low-tube-voltage, high-tube-current multidetector abdominal CT: improved image quality and decreased radiation dose with adaptive statistical iterative reconstruction algorithm—initial clinical experience. Radiology. 2010;254:145–53.
5. Pontana F, Duhamel A, Pagniez J, Flohr T, Faivre JB, Hachulla AL, et al. Chest computed tomography using iterative reconstruction vs filtered back projection (part 2): image quality of low-dose CT examinations in 80 patients. Eur Radiol. 2011;21:636–43.
6. Prakash P, Kalra MK, Digumarthy SR, Hsieh J, Pien H, Singh S, et al. Radiation dose reduction with chest computed tomography using adaptive statistical iterative reconstruction technique: initial experience. J Comput Assist Tomogr. 2010;34:40–5.
7. Yanagawa M, Honda O, Yoshida S, Kikuyama A, Inoue A, Sumikawa H, et al. Adaptive statistical iterative reconstruction technique for pulmonary CT: image quality of the cadaveric lung on standard- and reduced-dose CT. Acad Radiol. 2010;17:1259–66.
8. Leipsic J, Nguyen G, Brown J, Sin D, Mayo JR. A prospective evaluation of dose reduction and image quality in chest CT using adaptive statistical iterative reconstruction. AJR Am J Roentgenol. 2010;195:1095–9.
9. Hara AK, Paden RG, Silva AC, Kujak JL, Lawder HJ, Pavlicek W. Iterative reconstruction technique for reducing body radiation dose at CT: feasibility study. AJR Am J Roentgenol. 2009;193:764–71.
10. van Dijk AM, Martens JB. Subjective quality assessment of compressed images. Signal Process. 1997;58:235–52.
11. Miao J, Huo D, Wilson DL. Quantitative image quality evaluation of MR images using perceptual difference models. Med Phys. 2008;35:2541–53.
12. Escalante-Ramírez B, Martens J, de Ridder H. Multidimensional characterization of the perceptual quality of noise-reduced computed tomography images. J Vis Commun Image Represent. 1995;6:317–34.
13. Markarian B, Dailey ET. Preparation of inflated lung specimens. In: Heizman ER, editor. The lung: radiologic-pathologic correlations. 2nd ed. Mosby: St. Louis; 1984. p. 4–12.
14. Anderson NH. Algebraic models in perception. In: Carterette EC, Friedman MP, editors. Handbook of perception: volume 2, psychophysical judgment and measurement. 1st ed. New York: Academic Press; 1974. p. 215–98.
15. Slone RM, Foos DH, Whiting BR, Muka E, Rubin DA, Pilgram TK, et al. Assessment of visually lossless irreversible image compression: comparison of three methods by using an image-comparison workstation. Radiology. 2000;215:543–53.
16. Preston CC, Colman AM. Optimal number of response categories in rating scales: reliability, validity, discriminating power, and respondent preferences. Acta Psychol. 2000;104:1–15.
17. Singh S, Kalra MK, Gilman MD, Hsieh J, Pien HH, Digumarthy SR, et al. Adaptive statistical iterative reconstruction technique for radiation dose reduction in chest CT: a pilot study. Radiology. 2011;259:565–73.

Int J Cardiovasc Imaging (2012) 28:139–146
DOI 10.1007/s10554-010-9759-0

ORIGINAL PAPER

Relationship between beat to beat coronary artery motion and image quality in prospectively ECG-gated two heart beat 320-detector row coronary CT angiography

Nobuo Tomizawa · Shuhei Komatsu · Masaaki Akahane · Rumiko Torigoe · Shigeru Kiryu · Kuni Ohtomo

Received: 25 September 2010 / Accepted: 19 November 2010 / Published online: 30 November 2010

Abstract The objective was to investigate the influence of the beat-to-beat movement of the coronary arteries on image quality of multi-segment reconstruction (MSR) images. Although MSR improves temporal resolution, image quality would be degraded by beat-to-beat movement of the coronary arteries. In a retrospectively review, 18 patients (mean age, 67.0 years) who underwent coronary CT angiography using a 320-detector row CT were included. The displacement and diameter of coronary artery segments for each of the identified nine landmarks was recorded. The motion ratio was calculated as the division of displacement by diameter. Image quality (IQ) was graded by a four-point scale. The correlation between MSR IQ score and the motion ratio showed stronger negative correlation than that between MSR IQ score and the displacement ($r = -0.54$ vs. $r = -0.36$). The average motion ratio for segments in which half-scan reconstruction (HSR) IQ was better than MSR IQ (29.1%, group A) was higher than that for segments in which MSR IQ was better than HSR IQ (16.0%, group C). The motion ratio in group C was lower than 25%. Difference in IQ scores of the HSR images was more frequent in group A than in the remaining segments in which the motion ratio was lower than 25% (16.7% vs. 66.0%; $P < 0.0002$). The motion ratio could be a better index than the displacement to evaluate the influence of the motion of coronary arteries on image quality. MSR images would be impaired by a motion ratio larger than 25%. Image impairment of one of the HSR images might also impair MSR images.

Keywords Coronary CT angiography · Half-scan reconstruction · Image quality · Multi-segment reconstruction · Movement of coronary artery

N. Tomizawa (✉) · S. Komatsu · M. Akahane · K. Ohtomo
Department of Radiology, The University of Tokyo, 7-3-1 Hongo, 113-0033 Bunkyo-ku, Tokyo, Japan
e-mail: tomizawa-tky@umin.ac.jp

R. Torigoe
Toshiba Medical Systems Corporation, Tokyo Metropolitan Regional Office, 1-6 Tsukuda 2-Chome, 104-0051 Chuo-ku, Tokyo, Japan

S. Kiryu
Department of Radiology, Institute of Medical Science, The University of Tokyo, 4-6-1 Shirokanedai, 108-8639 Minato-ku, Tokyo, Japan

Introduction

Advances in computed tomography (CT) have improved image quality, leading to increased accuracy of diagnosis of coronary artery disease. Coronary CT angiography (CCTA) is indicated in several clinical pathologies due to its high negative predictive value [1–5]. The wide area of the detector in 320-detector row CT has enabled whole heart coverage in an axial (not helical) scan mode with one gantry

rotation. However, coronary arteries move and deform throughout the cardiac cycle, leading to degradation of image quality if temporal resolution is inadequate [6].

Temporal resolution is crucial for good image quality in CCTA [7, 8]. In order to improve temporal resolution, data from two or three cardiac cycles are used for image reconstruction which is called multi-segment reconstruction. When the gantry rotation time is 350 ms, temporal resolution of multi-segment reconstruction (MSR) images can be theoretically improved to 88 or 58 ms, respectively [9]. These are comparable to the temporal resolution of dual-source CT scanner (83 ms with single RR-cycle reconstruction and 42 ms with MSR algorithm) [10]. With some heart rates, benefits from improved temporal resolution with MSR might not offset the increased radiation dose and the decreased spatial resolution as the heart does not follow the same pattern of motion with every beat [8, 11]. Reconstruction algorithm that uses data from a single heart beat is called half-scan reconstruction algorithm. Although half-scan reconstruction (HSR) may result in lower radiation doses than MSR, images of patients with more rapid heart rate (HR) might be impaired due to the longer temporal resolution of HSR algorithm (approximately 175 ms when gantry rotation time is 350 ms).

There have been no studies that directly investigated coronary artery displacement and image quality in consecutive heart beats. Thus, the purpose of the present study was to investigate the influence of the beat-to-beat movement of the coronary arteries on image quality of MSR images.

Methods

Authors who are not employees of or consultants for Toshiba Medical Systems (Tokyo, Japan) had control of inclusion of any data and information that might present a conflict of interest for the author (R.T.), who is an employee of that company.

Patients

This retrospective study was approved by the local ethics committee, and the requirement for informed consent to participate this study was waived. In a retrospectively review, 23 consecutive patients (17 men, 6 women; mean age, 65.1 years ± 11.1; age range, 41–80 years) who underwent CCTA during November of 2009 were included in the analysis. All patients had clinical indications for CCTA and provided written informed consent for the examination. The patients were either suspected of having coronary artery disease (n = 18) or had a history of myocardial infarction with recurrent angina (n = 5). One patient with abnormal origin and course of a coronary artery was excluded from the study to minimize interfering factors affecting coronary artery motion. Four patients in whom the difference of R-R intervals exceeded 2% were also excluded in order to exclude the influence of HR variability. It is difficult to select the identical cardiac phase of the cardiac phase when R-R interval changes due to nonlinear changes in the time from the R wave to the various phases of the cardiac cycle as the heart rate varies [12]. We determined that 2% change of the R-R interval would have little influence on cardiac phase.

Thus the final study group included 18 patients (14 men, 4 women; mean age, 67.0 years ± 10.4; age range, 41–80 years) and a total of 21 exams.

CT data acquisition and postprocessing

All examinations were performed by using a 320-section CT scanner (Toshiba Aquilion ONE Dynamic Volume CT, Tochigi, Japan) with prospective ECG gating axial scans. The fraction of the R-R interval during which the patient was exposed ranged 65–85% for patients with lower HR [HR < 65 beats per minute (bpm)] and 30–80% for patients with higher HR (HR ≥ 65 bpm). The parameters were as follows: detector configuration, 320 × 0.5 mm; gantry rotation time, 350 or 375 ms depending on R-R time; tube potential, 120 kV; and tube current, ranging from 450 to 550 mA depending on body habitus. The effective radiation dose of CCTA was calculated as the product of the dose-length product times a conversion coefficient for the chest (k = 0.017 mSv/mGycm) [13]. Patients received 22.2 mgI/kg body weight/s of iopamidol 370 mgI/ml (Iopamiron 370, Bayer, Osaka, Japan, 54.6 ml ± 11.1; range, 38–79 ml) over 14 s. Bolus tracking in the ascending aorta was performed using a double threshold of 150 and 280 HU (Hounsfield unit). Patients were assigned to breathe in and hold their breaths after the first threshold. The scan

started just after the second threshold. Tatsugami et al. [14] showed that CCTA protocol using a double threshold yielded more consistent aortic enhancement with reduced interpatient variability than protocol using a single threshold.

One patient was receiving oral β-blocker as part of baseline medication. Oral β-blocker (20 mg of metoprolol) was indicated to 6 patients who had HR higher than 65 bpm at the outpatient department. The patients were assigned to take the medicine 2 h prior to the exam. No additional β-blocker was used when the HR was higher than 65 bpm at the time of the exam. There were no patients with contraindication to β-blockers, and there were no observed or reported side effects from β-blockers. All patients received 2.5 mg sublingual isosrobide dinitrate (Nitorol, Eisai, Tokyo, Japan) before imaging.

For each patient, the reconstruction phase with minimum artifact was determined at the CT console by reconstructing those 10 ms intervals available. Each exam contained three sets of images: HSR image of the first heart beat, HSR image of the second heart beat, and a two-beat MSR image.

CT data analysis

For data analysis, coronary segments were defined according to AHA guidelines [15]. Nine landmarks were identified in all reconstructed images (Fig. 1) and a multi-planar reconstruction image was generated on a cross-sectional plane for each landmark. Measurements were manually made by positioning a circular region of interest (ROI) and the x- and y-coordinates of the centroid of the circular ROI and the diameter were recorded. The ROI was placed three times and the average coordinates were used for evaluation. From these coordinates, the displacement of coronary artery motion was geometrically calculated in each HSR image using the following equation: displacement = $\left(\{x[h_1] - -x[h_2]\}^2 + \{y[h_1] - -y[h_2]\}^2\right)^{1/2}$, where h_1 and h_2 represent each HSR image. The motion ratio of coronary arteries was calculated as the division of displacement by diameter. The process described above was performed by one radiologist (N.T.).

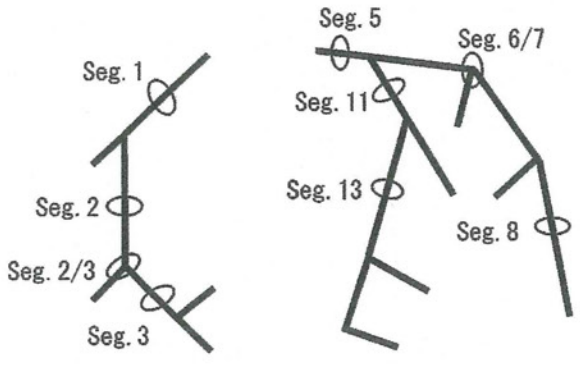

Fig. 1 Each landmark (*circle*) was identified at the mid-point of each segment. Nine landmarks were identified in all reconstructed images and a multi-planar reconstruction image was generated on a cross-sectional plane for each landmark

Image quality analysis

Two cardiovascular readers (N.T., S.-K.) independently rated coronary artery image quality. Before the reading session, the two readers determined by consensus image quality (IQ) scores defining the following four-point scale: 4, excellent, no artifact; 3, good, mild artifact; 2, acceptable, moderate artifact present but images still interpretable; 1, unable to evaluate, severe artifact renders interpretation not possible (Fig. 2). In the reading session, coronary arteries were shown patient by patient. For each patient, images were sorted in the order of coronary segment number in AHA guidelines. The three images of each landmark (2 HSR images and 1 MSR image) were displayed one by one randomly. The readers were blinded whether the images they were shown were HSR or MSR. When there was a difference in IQ scores between the two readers, the final IQ score was determined by consensus.

When the IQ score of at least one of the two HSR images was better than the score of MSR image, we defined HSR image better than MSR image (group A). Image quality of MSR image was considered better than that of HSR images when the IQ score of the MSR image was better than the scores of both HSR images (group C). Otherwise, image quality was considered equivalent (group B).

Statistical analysis

All statistical analyses were performed with commercially available statistical software (JMP, version 8.0.2; SAS, Cary, NC). Quantitative variables were expressed as means ± standard deviation.

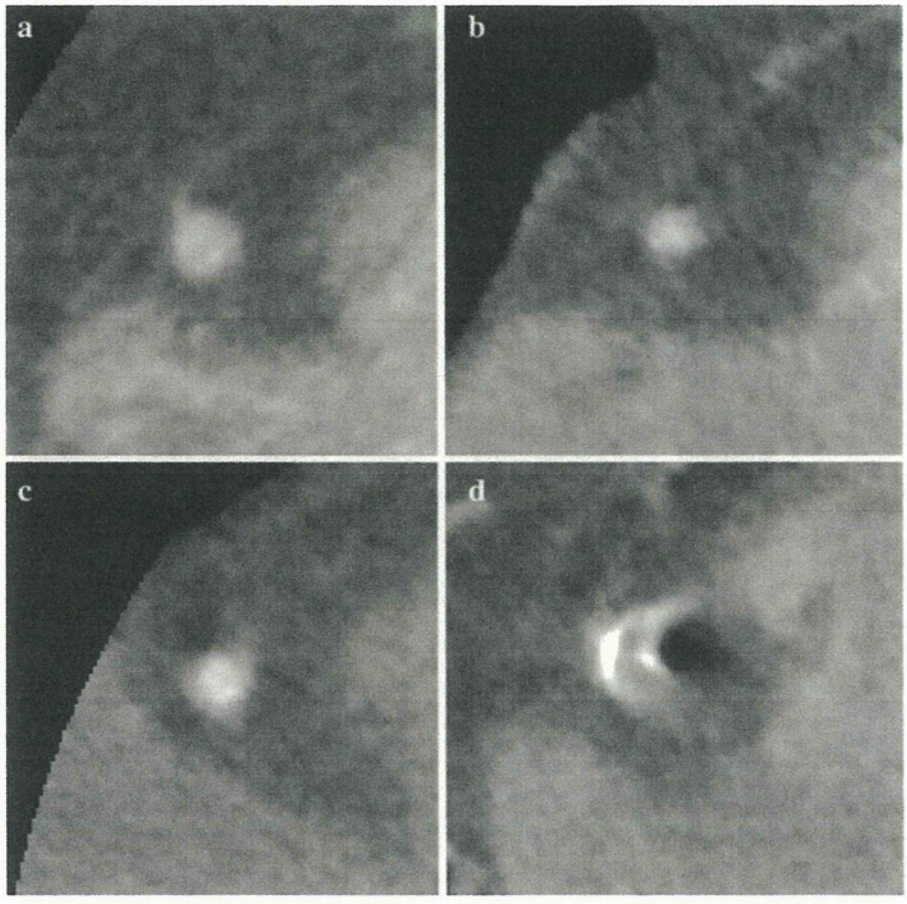

Fig. 2 Representative images through the mid-RCA illustrate the four image quality scores. 4, Excellent, no artifact (**a**); 3, Good, mild artifact (**b**); 2, Acceptable, moderate artifact present but images still interpretable (**c**); 1, Unable to evaluate, severe artifact renders interpretation not possible (**d**). Before the reading session, the two readers determined by consensus image quality scores. *RCA* right coronary artery

Interobserver agreement for image quality was calculated with Cohen κ statistics [16]. Result was interpreted as poor ($\kappa < 0.20$), fair ($\kappa = 0.21$–0.40), moderate ($\kappa = 0.41$–0.60), good ($\kappa = 0.61$–0.80), very good ($\kappa = 0.81$–0.90), or excellent ($\kappa \geq 0.91$).

The difference between the average IQ scores of HSR and MSR images of all exams was assessed by Welch's t test. Correlation of the motion ratio to HR, body mass index (BMI) and total body weight was analyzed by Spearman's rank-order correlation coefficients. The significance level was adjusted by Bonferroni to $0.05/3 = 0.017$. Correlation of MSR IQ score to the displacement and the motion ratio was also analyzed by Spearman's rank-order correlation coefficients. The significance level was adjusted by Bonferroni to $0.05/2 = 0.025$. The difference of the motion ratio between groups A–C was assessed by Steel–Dwass' test. Fisher's exact test was used to assess the frequency of the HSR IQ score difference between group A and groups B and C.

Results

Mean heart rate during scanning was 67.0 bpm ± 10.4 (range 51–89 bpm). The estimated mean dose-length product and the mean effective radiation dose was 918 mGycm ± 376 and 15.6 mSv ± 6.4 each.

Motion of coronary artery segments

Four of the possible 189 segments (21 exams × 9 segments per exam) were either not present (n = 1)

Table 1 Summary of average displacement, diameter, and motion ratio in each coronary artery segment

Coronary segment	Displacement (mm)	Diameter (mm)	Motion ratio (%)
#1	0.60 ± 0.36	4.2 ± 0.7	14 ± 7
#2	0.63 ± 0.31	4.0 ± 0.6	16 ± 8
#2/3	0.65 ± 0.41	3.5 ± 0.7	20 ± 15
#3	0.64 ± 0.48	3.1 ± 0.8	21 ± 15
#5	0.48 ± 0.30	4.7 ± 1.1	11 ± 8
#6/7	0.38 ± 0.21	3.7 ± 0.7	11 ± 8
#8	0.49 ± 0.39	2.3 ± 0.3	22 ± 16
#11	0.50 ± 0.51	3.5 ± 0.7	16 ± 19
#13	0.44 ± 0.38	2.4 ± 0.7	20 ± 20

Data are average ± standard deviations

or poorly imaged due to a stent inside (n = 1) or occluded (n = 2) limiting measuring coordinates. A summary of average displacement, diameter and the motion ratio is shown in Table 1. There was no significant relationship between average motion ratio and HR (r = 0.17; $P = 0.47$), BMI (r = 0.057; $P = 0.80$) and total body weight (r = 0.07; $P = 0.77$) for each exam.

Image quality of coronary artery segments

Interobserver agreement was interpreted as "very good" ($\kappa = 0.82$). Four of the possible 189 segments were either occluded (n = 2), had a stent inside (n = 1), or were not present (n = 1), limiting evaluation.

For MSR images, images without artifacts (score 4) were obtained in 103 segments (55.7%); images with mild artifacts (score 3) in 64 segments (34.6%); images with moderate artifacts (score 2) in 14 segments (7.6%); and images with severe artifacts (score 1) in 4 segments (2.2%). For HSR images, 196 segments (53.0%) were rated as score 4, 121 segments (32.7%) as score 3, 42 segments (11.4%) as score 2, and 11 segments (3.0%) as score 1.

IQ scores of HSR and MSR images on a per-segment basis are shown in Table 2. Average IQ scores were not significantly different ($P = 0.28$) between HSR and MSR images. There was a significant negative correlation between MSR IQ score and the displacement of coronary artery segments (r = −0.36; $P = 0.018$) (Fig. 3a). The correlation between MSR IQ score and the motion ratio showed a stronger negative correlation (r = −0.54; $P = 0.0002$) (Fig. 3b).

Table 2 IQ scores of MSR and HSR images on a per-segment basis

Coronary segment	MSR IQ score	HSR IQ score
#1	3.8 ± 0.4	3.5 ± 0.7
#2	3.0 ± 0.7	2.9 ± 0.9
#2/3	3.2 ± 0.9	3.3 ± 0.9
#3	3.4 ± 0.7	3.4 ± 0.7
#5	3.8 ± 0.4	3.8 ± 0.5
#6/7	3.7 ± 0.6	3.6 ± 0.6
#8	3.1 ± 0.8	3.0 ± 0.9
#11	3.7 ± 0.6	3.6 ± 0.6
#13	3.3 ± 0.8	3.1 ± 0.8
Average	3.4 ± 0.7	3.4 ± 0.8

Data are average ± standard deviations

IQ image quality, *MSR* multi-segment reconstruction, *HSR* half-scan reconstruction

Thirty-seven segments (20.0%) were included in group A, 133 segments (71.9%) in group B and 15 segments (8.1%) in group C. Of the 109 segments in which the IQ scores of the two HSR images were equivalent, 14 segments (12.8%) were included in group A, 85 segments (78.0%) in group B and 10 segments (9.2%) in group C.

Effect of motion ratio on image quality

The motion ratio for group A was 29.1% ± 17.3; that for group B was 13.5% ± 11.6; and that for group C was 16.0% ± 6.3. The motion ratio for group A was significantly larger than that for group B ($P < 0.05$). The motion ratio for all segments in group C was lower than 25% (Fig. 4).

Effect of difference in HSR IQ scores on MSR IQ score

Of the 151 segments in which the motion ratio was lower than 25%, 18 (11.9%) segments were included in group A. The HSR IQ scores were equivalent in 3 (16.7%) of the 18 segments. Of the remaining 133 segments, the HSR IQ scores were equivalent in 88 (66.0%) segments. Difference in IQ scores was more frequent in segments of group A than in the remaining segments in which the motion ratio was lower than 25% ($P < 0.0002$).

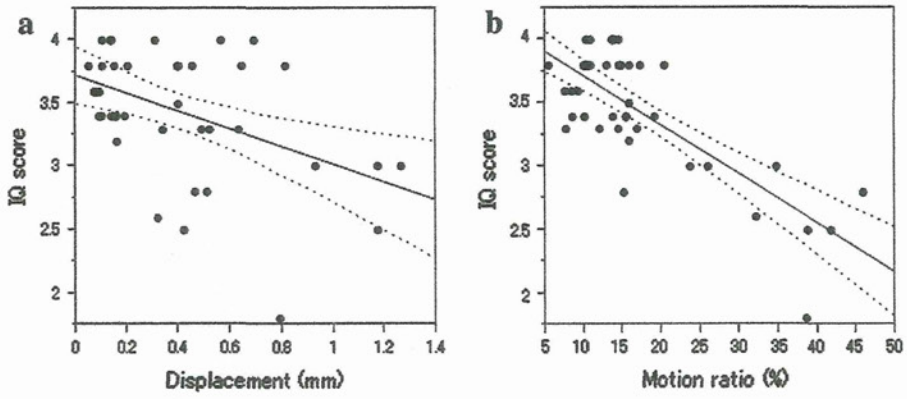

Fig. 3 Scattergram shows relationship between MSR IQ score and the movement of the coronary arteries. *Solid lines* show linear regression. *Dotted lines* represent 95% confidence limits. Each plot represents the average value of RCA (#1, #2, #2/3, #3) and LCA (#5, #6/7, #8, #11, #13) in each exam. Correlation between MSR IQ score and the displacement was −0.36 ($P = 0.018$), indicating statistically significant negative correlation (**a**). However, the correlation between MSR IQ score and the motion ratio was −0.54 ($P = 0.0002$), indicating stronger negative correlation than the correlation between MSR IQ score and displacement (**b**). The motion ratio would be a better index to evaluate the effect of the motion of coronary arteries on image quality. *MSR* multi-segment reconstruction, *IQ* image quality, *RCA* right coronary artery, *LCA* left coronary artery

Discussion

Rapid motion of the heart degrades the image quality of coronary arteries in CCTA [7]. The present study showed that there was a negative relationship between MSR IQ score and the displacement of coronary arteries in consecutive two beats. However, the negative relationship was stronger between MSR IQ score and the motion ratio. The motion ratio is calculated by dividing the displacement by the diameter of the coronary artery segment, such that smaller coronary artery segment has a higher motion ratio when the absolute displacement is the same. The results in the present study show that the image quality of smaller segments could be more vulnerable to cardiac motion. Thus we used the motion ratio as an index to evaluate the effect of the motion of coronary arteries on image quality.

The present study showed that IQ scores of MSR images would be degraded when the motion ratio is above 25%. Although the average motion ratio was higher in group A than in group C, the difference was not significant. The reason for this could be because the difference in the image quality of HSR images could also impair the image quality of MSR images as discussed later. However, we could not find a relationship between motion ratio and HR, BMI and total body weight. Sebastian et al. [17] showed a strong correlation between variability (i.e., standard deviation) of HR during scanning and mean image quality. Their study showed that image quality was significantly better in patients with low variability in HR. In the present study, patients were included whose variability of R-R interval was lower than 2%; hence, further investigation is required to find relationship between the motion ratio and variability of R-R intervals. It is difficult to know beforehand which factor causes a higher motion ratio.

Even when the motion ratio was lower than 25%, 11.9% of all segments were included in group A. The difference in IQ scores in HSR images in a single segment was more frequent in segments which were included in group A when the motion ratio was lower than 25% than in the remaining segments in which the motion ratio was lower than 25%. Thus, image quality of MSR images might be degraded when one of the HSR images is impaired. It is clinically known that there are nonlinear changes in the time from the R wave to the various phases of the cardiac cycle as the heart rate varies (i.e., the diastolic phases are more sensitive to changes in heart rate than systole) [12]. However, the cardiac phase would be the same when the R-R interval is unchanged. The present results imply that cardiac phase might change even if heart rates do not change. There might be other causes which could lead to the difference of IQ scores. During acquisition of the latter beat, residual contrast agent in the right ventricle decreases

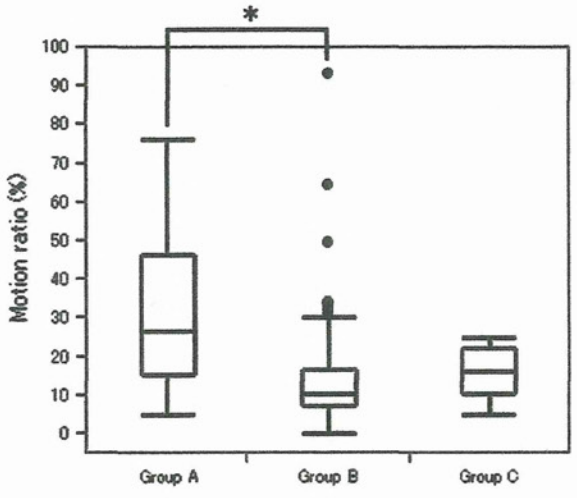

Fig. 4 When the IQ score of at least one of the two HSR images was better than the score of MSR image, we defined HSR image better than MSR image (group A). Image quality of MSR image was considered better than that of HSR images when the IQ score of the MSR image was better than the scores of both HSR images (group C). Otherwise, image quality was considered equivalent (group B). All plots in group C were lower than 25%, thus IQ scores of MSR images would be degraded when the motion ratio is above 25%. Although the average motion ratio was higher in group A than in group C, the difference was not significant. The reason for this could be because the difference in the image quality of HSR images could also impair the image quality of MSR images. Note *Box* 1st–3rd quartiles, *bold line* median, *whiskers* minimum and maximum values, *filled circle* outlier, *asterisk* statistically significant ($P < 0.05$). *IQ* image quality, *HSR* half-scan reconstruction, *MSR* multi-segment reconstruction

compared to the former beat. Horiguchi et al. [18] showed that heart rate varies immediately after breath hold and that 4 or 5 s after breath hold is recommended before starting cardiac CT examination. Further study is necessary to investigate whether these factors have influence on image quality of the HSR images.

The present study does not suggest MSR has no advantage and therefore should be avoided in this 320-slice CT scanner. Previous studies have shown that MSR improves image quality in higher heart rates [8, 19, 20]. In the present study, the image quality was equivalent with HSR and MSR images in 71.9% of all segments. The reason for this could be because the average HR was 67.0 bpm. Herzog et al. [19] showed that MSR benefits only at certain heart rates. This is because the time resolution oscillates between half and quarter of the gantry rotation time depending on heart rate [10, 19, 21]. Herzog et al. used the same helical pitch and gantry rotation time in all patients, hence the heart rate in which the MSR benefits was limited. The time resolution of MSR could be improved in various heart rates by changing the gantry rotation time in 320-detector CT with heart rate of each patient. The present study showed that motion of coronary arteries could also impair MSR image quality. Further study is needed to investigate the factor which causes higher movement of coronary arteries thus improving the image quality of MSR images.

There were some limitations in this study. By employing a limited number of landmarks on coronary arteries, we have provided descriptions of coronary artery motion only at selected points. However, motion of coronary arteries is non-uniform and is characterized by changes in the magnitude and direction of vessel motion and axial strain [22, 23].

A third of this study population was receiving β-blocker medications. Therefore, in the present study population, actual coronary movements may have been underestimated. Patients with various degrees of cardiac disease were included. The degree of impairment in ventricular motion caused by myocardial disease would lead to deviations of the motion patterns.

This study was restricted in two-dimensional analysis. Coronary artery segments were assessed on a single plane. Coronary arteries move in a three-dimensional way; thus, the present data do not show the exact movement of each segment. In order to assess the movement for each segment, bifurcation points need to be identified as landmarks.

Finally, the time resolution for MSR images was not analyzed. By using two-beat MSR, temporal resolution oscillates between one-half and one-fourth of the gantry rotation time, depending on the heart rate [11, 21].

In conclusion, the motion ratio could be a better index than the displacement to evaluate the influence of the motion of coronary arteries on image quality. MSR images would be impaired by a motion ratio larger than 25%. Image impairment of one of the HSR images might also impair MSR images. However, there was no significant relationship between the motion ratio and HR, BMI and total body weight. Further study is necessary to investigate factors which may influence on the movement in consecutive heart beats.

Acknowledgments We have not received any funding for this study.

References

1. Hendel RC, Kramer CM, Patel MR, Poon M (2006) ACCF/ACR/SCCT/SCMR/ASNC/NASCI/SCAI/SIR 2006 Appropriateness criteria for cardiac computed tomography and cardiac magnetic resonance imaging. A report of the American College of Cardiology Foundation Quality Strategic Directions Committee Appropriateness Criteria Working Group, American College of Radiology, Society of Cardiovascular Computed Tomography, Society for Cardiovascular Magnetic Resonance, American Society of Nuclear Cardiology, North American Society for Cardiac Imaging, Society for Cardiovascular Angiography and Interventions, and Society of Interventional Radiology. J Am Coll Cardiol 48:1475–1497
2. Vanhoenacker PK, Heijenbrok-Kal MH, Van Heste R et al (2007) Diagnostic performance of multidetector CT angiography for assessment of coronary artery disease: meta-analysis. Radiology 244:419–428
3. Scheffel H, Alkadhi H, Plass A et al (2006) Accuracy of dual-source CT coronary angiography: first experience in a high pre-test probability population without heart rate control. Eur Radiol 16:2739–2747
4. Mollet NR, Cademartiri F, van Mieghem CA et al (2005) High-resolution spiral computed tomography coronary angiography in patients referred for diagnostic conventional coronary angiography. Circulation 112:2318–2323
5. Dewey M, Zimmermann E, Deissenrieder F et al (2009) Noninvasive coronary angiography by 320-row computed tomography with lower radiation exposure and maintained diagnostic accuracy. Circulation 120:823–824
6. Ding Z, Friedman MH (2000) Quantification of 3-D coronary arterial motion using clinical biplane cineangiograms. Int J Card Imaging 16:331–346
7. Achenbach S. (2007) CT coronary angiography. Half-Scan vs. multi-segment reconstruction for computed tomography coronary angiography. SOMATOM Sessions. http://www.medical.siemens.com/siemens/en_US/cs_cardio_FBAs/files/Case_Study/Achenbach_MultiSegment_Reconstruction.pdf. Accessed 4 September 2010
8. Halliburton SS, Stillman AE, Flohr T et al (2003) Do segmented reconstruction algorithms for cardiac multislice computed tomography improve image quality? Herz 28:20–31
9. Kitagawa K, Lardo AC, Lima JAC, George RT (2009) Prospective ECG-gated 320 row detector computed tomography: implications for CT angiography and perfusion imaging. Int J Cardiovasc Imaging 25:201–208
10. Achenbach S, Ropers D, Kuettner A et al (2006) Contrast-enhanced coronary artery visualization by dual-source computed tomography—initial experience. Eur J Radiol 57:331–335
11. Flohr T, Ohnesorge B (2001) Heart rate adaptive optimization of spatial and temporal resolution for electrocardiogram-gated multislice spiral CT of the heart. J Comput Assist Tomogr 25:907–923
12. Vembar M, Garcia MJ, Heuscher DJ et al (2003) A dynamic approach to identifying desired physiological phases for cardiac imaging using multislice spiral CT. Med Phys 30:1683–1693
13. Einstein AJ, Moser KW, Thompson RC et al (2007) Radiation dose to patients from cardiac diagnostic imaging. Circulation 116:1290–1305
14. Tatsugami F, Matsuki M, Shigesato H et al. A new imaging technique using real prep with 320 detector coronary CT angiography [article in Japanese]. Paper presented at: Meeting of Japan Society of Cardiovascular Radiology, Kumamoto, Japan, 3 July 2010
15. Austen WG, Edwards JE, Frye RL et al (1975) A reporting system on patients evaluated for coronary artery disease: report of the Ad Hoc Committee for grading of coronary artery disease, council on cardiovascular surgery, American Heart Association. Circulation 51:5–40
16. Cohen J (1960) A coefficient of agreement for nominal scales. Educ Pshychol Meas 20:37–46
17. Leschka S, Wildermuth S, Boehm T et al (2006) Noninvasive coronary angiography with 64-section CT: effect of average heart rate and heart rate variability on image quality. Radiology 241:378–385
18. Horiguchi J, Yun S, Hirai N et al (2006) Timing on 16-slice scanner and implications for 64-slice cardiac CT: do you start scanning immediately after breath hold? Acad Radiol 13:173–176
19. Herzog C, Nguyen SA, Savino G et al (2007) Does two-segment image reconstruction at 64-section CT coronary angiography improve image quality and diagnostic accuracy? Radiology 244:121–129
20. Wang YT, Yang CY, Hsiao JK et al (2009) The influence of reconstruction algorithm and heart rate on coronary artery image quality and stenosis detection at 64-detector cardiac CT. Korean J Radiol 10:227–234
21. Ebert TJ, Eckberg DL, Vetrovec GM et al (1984) Impedance cardiograms reliably estimate beat-by-beat changes of left ventricular stroke volume in humans. Cardiovasc Res 18:354–360
22. Ding Z, Friedman MH (2000) Dynamics of human coronary arterial motion and its potential role in coronary atherogenesis. J Biomech Eng 122:488–492
23. Duerinckx A, Atkinson DP (1997) Coronary MR angiography during peak-systole: work in progress. J Magn Reson Imaging 7:979–986

Journal of Cardiovascular Computed Tomography (2012) 6, 318–324

Journal of Cardiovascular Computed Tomography

Original Research Article

Adaptive Iterative Dose Reduction in coronary CT angiography using 320-row CT: Assessment of radiation dose reduction and image quality

Nobuo Tomizawa, MD[a,*], Takeshi Nojo, MD[a], Masaaki Akahane, MD[a], Rumiko Torigoe, RT[b], Shigeru Kiryu, MD[c], Kuni Ohtomo, MD[a]

[a]Department of Radiology, The University of Tokyo, 7-3-1 Hongo, Bunkyo-ku, Tokyo 113-0033, Japan; [b]Toshiba Medical Systems Corporation, Tokyo Metropolitan Regional Office, Tokyo, Japan and [c]Department of Radiology, Institute of Medical Science, The University of Tokyo, Tokyo, Japan

KEYWORDS:
Coronary CT angiography;
Effective dose;
Filtered back projection;
Iterative reconstruction;
320-row CT

BACKGROUND: Several methods have been developed to reduce the radiation dose in coronary computed tomography angiography (CTA).

OBJECTIVE: The objective of our study was to evaluate the effects of Adaptive Iterative Dose Reduction (AIDR) on objective and subjective image quality as well as the radiation dose, compared with conventional filtered back projection (FBP), in coronary CTA.

METHODS: We retrospectively reviewed 100 consecutive patients who underwent coronary CTA. In the first 50 patients, a higher tube current was used, and images were reconstructed with FBP. In the last 50 patients, a lower tube current was used, and images were reconstructed with AIDR. Subjective and objective image quality (noise, signal-to-noise ratio, contrast-to-noise ratio) were assessed.

RESULTS: The median radiation dose of the AIDR group was 22% lower than that of the FBP group (4.2 vs 5.4 mSv; $P = 0.0001$). No significant difference was found in subjective image quality, noise, signal-to-noise ratio, or contrast-to-noise ratio between the 2 groups.

CONCLUSION: AIDR reduced the tube current which resulted in reduction of radiation dose in coronary CTA while maintaining subjective and objective image quality compared with coronary CTA reconstructed with FBP.

Introduction

Significant advances in coronary computed tomography angiography (CTA) have allowed noninvasive evaluation of the heart and coronary arteries.[1] Coronary CTA requires high spatial resolution and low noise, which are accomplished with various radiation doses across patients and imaging facilities (1−20 mSv).[2] Several methods have been developed to reduce the radiation dose to meet the "as low as reasonably achievable principle" for coronary CTA.[2,3] These methods include electrocardiogram-based tube current modulation for helical examinations,[2–5] prospective gating,[2,4,5] noise reduction filters,[4] high-pitch spiral acquisition,[2,5] reduction of tube voltage,[2,3,5] and reduction of z-axis scan length.[2,3]

Conflict of interest: The authors report no conflicts of interest.

* Corresponding author.
E-mail address: tomizawa-tky@umin.ac.jp

Submitted November 13, 2011. Accepted for publication February 27, 2012.

1934-5925/$ - see front matter © 2012 Society of Cardiovascular Computed Tomography. All rights reserved.
http://dx.doi.org/10.1016/j.jcct.2012.02.009

Connective Tissue Research, 2012; 53(5): 349–354
Copyright © Informa Healthcare USA, Inc.
ISSN: 0300-8207 print/1607-8438 online
DOI: 10.3109/03008207.2012.657309

informa
healthcare

Differential Expression of Wound Fibrotic Factors between Facial and Trunk Dermal Fibroblasts

Masakazu Kurita,[1] Mutsumi Okazaki,[2] Akiko Kaminishi-Tanikawa,[1] Mamoru Niikura,[3] Akihiko Takushima,[1] Kiyonori Harii[1]

[1]*Department of Plastic Surgery, Kyorin University School of Medicine, Tokyo, Japan,* [2]*Department of Plastic and Reconstructive Surgery, Graduate School, Tokyo Medical and Dental University, Tokyo, Japan,* [3]*Department of Parasitology, Kyorin University School of Medicine, Tokyo, Japan*

Clinically, wounds on the face tend to heal with less scarring than those on the trunk, but the causes of this difference have not been clarified. Fibroblasts obtained from different parts of the body are known to show different properties. To investigate whether the characteristic properties of facial and trunk wound healing are caused by differences in local fibroblasts, we comparatively analyzed the functional properties of superficial and deep dermal fibroblasts obtained from the facial and trunk skin of seven individuals, with an emphasis on tendency for fibrosis. Proliferation kinetics and mRNA and protein expression of 11 fibrosis-associated factors were investigated. The proliferation kinetics of facial and trunk fibroblasts were identical, but the expression and production levels of profibrotic factors, such as extracellular matrix, transforming growth factor-β1, and connective tissue growth factor mRNA, were lower in facial fibroblasts when compared with trunk fibroblasts, while the expression of antifibrotic factors, such as collagenase, basic fibroblast growth factor, and hepatocyte growth factor, showed no clear trends. The differences in functional properties of facial and trunk dermal fibroblasts were consistent with the clinical tendencies of healing of facial and trunk wounds. Thus, the differences between facial and trunk scarring are at least partly related to the intrinsic nature of the local dermal fibroblasts.

Keywords: fibrosis, scarring, fibroblast, heterogeneity, tissue specificity

Introduction

Fibroblasts are the most common cells present in connective tissues, where they synthesize extracellular matrix (ECM) and play a critical role in wound healing [1]. Fibroblasts are known to be composed of diverse cell populations and manifest phenotypic differences in their function, such as ECM production and organization, and production of growth factors and cytokines [2–5]. These differences in properties are notable in cutaneous pathological conditions such as keloid [6], hypertrophic scar [7], scleroderma [8], café au lait macule [9], and neurofibroma [10], and even under physiological conditions, fibroblasts exhibit differences; this is known as fibroblast heterogeneity [3–5]. The functional differences are particularly evident between superficial dermal fibroblasts and deep dermal fibroblasts [3–5,11–15]. Heterogeneity also exists between anatomical locations, as several recent studies have indicated that fibroblasts from different body sites retain positional information and topographic differentiation patterns in the expression of genes in vitro [16,17]. However, there are limited reports of the differences in wound healing-associated functions between dermal fibroblasts based on body sites [18].

Clinically, wounds on the face and trunk show different tendencies for wound scarring [19]. Facial incisional wounds, particularly preauricular incisional wounds, heal with less scarring than similar wounds on the trunk. Factors such as the innate properties of resident cells, thickness and compositional structure of the dermis, perfusing blood flow, and mechanical stresses such as skin tension are thought to be the reasons for such differences [19,20]. However, to our knowledge, no studies have elucidated the specific mechanisms responsible.

In order to clarify whether the characteristic properties of facial and trunk scarring are due to differences in local fibroblasts, functional differences between facial dermal fibroblasts and trunk dermal fibroblasts were investigated, using primary facial superficial dermal fibroblasts (FS), facial deep dermal fibroblasts (FD), trunk superficial dermal fibroblasts (TS), and trunk deep dermal fibroblasts (TD). Thus, cellular proliferation kinetics, and expression and production of 11 fibrosis-associated factors, including representative ECM metabolism-associated factors or cytokines, which are considered to be related to scar fibrosis, were investigated and compared between facial and trunk dermal fibroblasts.

Materials and Methods

Cell Isolation and Culture

Facial (preauricular) and trunk (lateral thoracic) skin was obtained during reconstructive surgery from seven healthy donors without antecedent operative invasion to the biopsied site (four females and three males; age, 46.6 ± 14.4 years). Profiles and data description codes are shown in Table 1. The research protocol was approved by the internal review board of our university hospital. Informed consent was obtained from all patients. After resection of subcutaneous tissues, specimens were washed three times in phosphate-buffered saline, and the external and internal surfaces were dermatomed in order to obtain superficial and deep dermal samples, respectively. To avoid cellular selection bias, both

Address correspondence to Masakazu Kurita, MD, PhD, Department of Plastic Surgery, Kyorin University School of Medicine, 6-20-2 Shinkawa, Mitaka-shi, Tokyo 181-8611, Japan. Tel.: +81-422-47-5511; Fax: +81-422-46-0138. E-mail: masakazukurita@aol.com
Received 31 October 2011; Revised 9 January 2012; Accepted 10 January 2012

Table 1. Profiles and data description codes of samples

No.	Age	Sex	Proliferation assay	Real-time PCR assay	ELISA (collagen I)	ELISA (cytokines)	Symbol in figures
1	44	M	*	*	*	*	○
2	34	M	*	*	*	*	△
3	60	F	*	*	*	*	□
4	65	M	*	*	*	*	•
5	53	F	*	*	*	*	▲
6	24	F	*	*		*	■
7	46	F	*	*			×

samples were incubated with 0.25% trypsin and 0.02% EDTA in phosphate-buffered saline for 16–24 hr at 4°C and the epithelium was separated from the superficial dermal sample. From the separated superficial and deep dermal samples, human fibroblasts were cultured as explants and maintained at 37°C under a 5% CO_2 atmosphere in fibroblast growth medium (FGM) consisting of Dulbecco's modified Eagle's medium (DMEM) supplemented with 10% fetal calf serum and 0.6 mg/ml glutamine. After about 3 weeks, primary cultures were subcultured. Medium was replaced every 3 days during cell culture.

Proliferation Assay

Cells at the third passage were plated in triplicate in 12-well plates at 1.0×10^4 cells/well in FGM. Medium was replaced every 4 days and the cell number was manually counted at the same time until day 32.

Quantification of mRNA by Real-Time Polymerase Chain Reaction

Cells at four or five passages were plated in 12-well plates at 1.0×10^4 cells/well in FGM. On day 4, total RNA was isolated using an RNeasy™ Mini Kit and QIA shredder (both from QIAGEN, Hilden, Germany), followed by reverse transcription using a High Capacity RNA-to-cDNA kit. Wound maturation-associated genes (listed in Table 2) were quantified using real-time polymerase chain reaction (PCR). Reaction mixtures comprised 10 µl of FAST SYBR® Green Master Mix and 1 µl of cDNA sample and RNase-free water with the indicated primer concentrations. Reactions were performed and monitored using the StepOnePlus™ real-time PCR system. All PCR reagents and the PCR system were obtained from Applied Biosystems (Foster City, CA, USA). PCR comprised 40 cycles, consisting of denaturing at 95°C (3 s) and annealing/extension at 60°C (15 s). Primer sequences were designed based on previous studies and were optimized for concentration [8,21–25]. Primers for which amplification efficiency was between 1.95 and 2.05 were employed for the study. Sequences and optimized concentrations for each primer are shown in Table 2. For quantification, expression levels were calculated by the comparative CT method using glyceraldehyde-3-phosphate dehydrogenase (GAPDH) and human acidic ribosomal protein (HARP) as an endogenous reference gene. Preliminary tests confirmed that both the endogenous controls offered similar results. Therefore, we decided to use GAPDH as an internal control throughout the study.

Measurement of ECM and Cytokines by Enzyme-Linked Immunesorbent Assay

Samples for enzyme-linked immunesorbent assay (ELISA) were collected under the same culture conditions as cDNA. Soluble and sediment type I collagens were quantitatively analyzed by ELISA (Human collagen I EIA kit; Applied Cell Biotechnologies, Inc., Yokohama, Kanagawa, Japan) according to the manufacturer's instructions. Transforming growth factor-β1 (TGF-β1), transforming growth factor-β2 (TGF-β2), and connective tissue growth factor (CTGF) in culture supernatants were also measured by ELISA (Quantikine™ from R&D Systems (Minneapolis, MN, USA) for TGF-β1 and TGF-β2, and Human CTGF ELISA Kit from Cusabio, Inc., Wuhan, Hubei, China, for CTGF), in accordance with the manufacturer's instructions. Levels of each factor were measured using a microplate reader (Power Scan® HT; Dainippon Pharmaceutical, Osaka, Japan). Data are expressed as secreted factors per 1.0×10^4 cells at the time of harvest.

Statistical Analyses

Differences in values between groups of cells were analyzed by paired Student's *t*-test. In the proliferation assay, associations between cell number of facial dermal fibroblasts and trunk dermal fibroblasts at confluence (on day 32) were statistically analyzed using Pearson's correlation index. Values of $p < 0.05$ were considered to be statistically significant. Chronological changes in cell number are presented as means ± standard error of the mean, and other data are presented as means ± standard deviation.

Results

Cell Morphology and Proliferation

Morphologically, no differences were observed between dermal fibroblasts obtained from the face and trunk, while superficial dermal fibroblasts and deep dermal fibroblasts showed apparent differences regardless of donor site. Superficial dermal fibroblasts were smaller and spindle-shaped when compared with deep dermal fibroblasts, which tended to broadly spread on the surface (Figure 1). In addition, with regard to proliferation kinetics, no differences were observed between facial and trunk dermal fibroblasts, although the cellular density of superficial dermal fibroblasts tended to be higher than that of deep dermal fibroblasts on proliferation assay (Figure 2A), as shown in the comparative description of cell numbers of FS, FD, TS, and TD on day 32 (Figure 2B). Cell numbers at confluency on day 32 demonstrated that for superficial dermal fibroblasts and deep dermal fibroblasts, respectively, cellular density of facial and trunk dermal fibroblasts from the same donor showed significant correlations (Figure 2C).

mRNA Expression of Fibrosis-Associated Factors

In order to investigate the functional differences between facial and trunk dermal fibroblasts, mRNA expression of fibrosis-associated factors in superficial dermal fibroblasts and deep dermal fibroblasts was quantitatively compared using real-time PCR.

Among superficial dermal fibroblasts, FS showed lower expression of ECMs such as type I and III collagens, fibronectin, TGF-β1 and TGF-β3, and CTGF when compared with TS. On the other

Table 2. Primer sequences and optimized concentrations for real-time PCR

Gene	Coding protein	Sequence	Primer concentration [nM]
COL1A1	Type I collagen	F: CCCACCAATCACCTGCGTACAGA	100
		R: TTCTTGGTCGGTGGGTGACTCTGA	100
COL3A1	Type III collagen	F: GAGATGTCTGGAAGCCAGAACCAT	100
		R: GATCTCCCTTGGGGCCTTGAGGT	100
FN1	Fibronectin	F: GGAGAATTCAAGTGTGACCCTCA	300
		R: TGCCACTGTTCTCCTACGTGG	300
MMP1	MMP1 (collagenase)	F: TCTGGGGTGTGGTGTCTCA	300
		R: GCCTCCCATCATTCTTCAGGTT	300
TGFB1	TGF-β1	F: GTTCAAGCAGAGTACACACAGC	300
		R: GTATTTCTGGTACAGCTCCACG	300
TGFB2	TGF-β2	F: ATGCGGCCTATTGCTTTAGA	200
		R: TAAGCTCAGGACCCTGCTGT	200
TGFB3	TGF-β3	F: CAGGGAGAAAATCCAGGTCA	100
		R: CCTGGAAGGCGTCTAACCAAG	100
CTGF	CTGF	F: ACGGCGAGGTCATGAAGAAGAACA	100
		R: ACTCTCTGGCTTCATGCCATGTCT	100
ASMA	α-smooth muscle actin	F: CCAAGCACTGTCAGGAAT	100
		R: AGGCAGTGCTGTCCTCTT	100
FGF2	bFGF	F: ATACAGCAGCAGCCTAGCAACTCT	100
		R: TTCGGCAACAGCACACAAATCCTG	100
HGF	HGF	F: GCAAGTGAATGGAAGTCCTTTA	100
		R: CAGAGGGACAAAGGAAAAGAA	100
SCF	SCF	F: GCCGCTGTTCGTGCAATAT	200
		R: CTGCGATCCAGCACAAACAGT	200
HARP	HARP	F: CGCTGCTGAACATGCTCAA	300
		R: TGTCGAACACCTGCTGGATG	300
GAPDH	GAPDH	F: GAAGGTGAAGGTCGGAGTC	300
		R: GAAGATGGTGATGGGATTTC	300

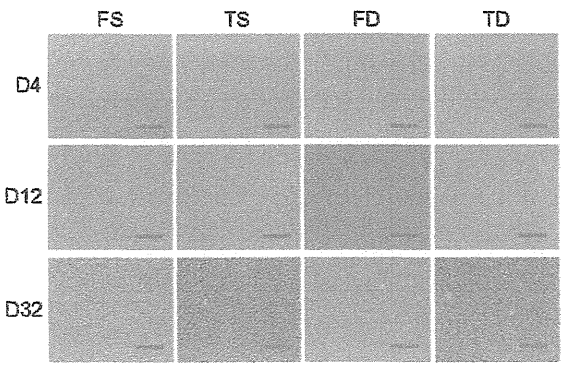

Figure 1. Cell morphology of FS, TS, FD, and TD. Phase contrast microscopic findings for FS, TS, FD, and TD from donor No. 4 at 4, 12, and 32 days after cell seeding. Scale bar indicates 100 μm.

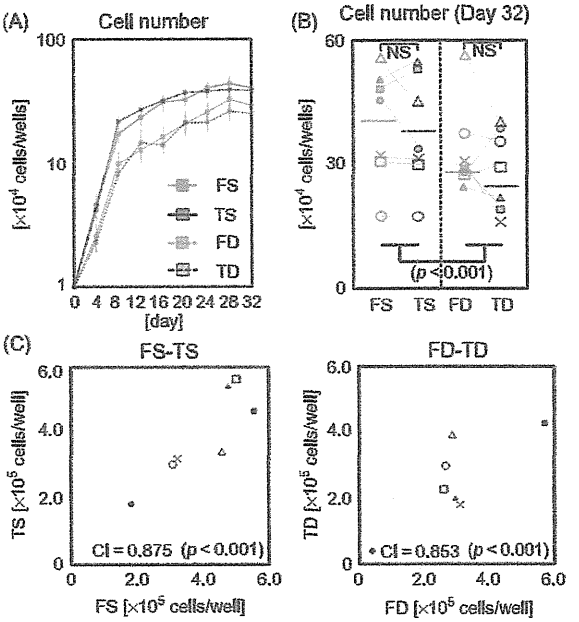

Figure 2. Cell proliferation of FS, TS, FD, and TD. (A) Chronological cell number in four cell fractions is noted ($n = 7$ for each). Error bars indicate SEM. (B) Cell count of FS, TS, FD, and TD on day 32 ($n = 7$ for each). (C) Correlation of saturated cell number between facial and trunk fibroblasts on day 32.

hand, expression of TGF-β2 was higher in FS than in TS. Expression of MMP1, ASMA, bFGF, and HGF showed no clear trends. Among deep dermal fibroblasts, FD showed lower expression of TGF-β1 and CTGF than TD, while no clear trends were seen for other factors (Figure 3).

Production of Fibrosis-Associated Factors

In order to further confirm the differences between facial and trunk dermal fibroblasts, protein production of type I collagen, TGF-β1, TGF-β2, and CTGF were compared by ELISA.

Among superficial dermal fibroblasts, FS showed significantly lower production of type I collagen, TGF-β1, and CTGF than TS. this was consistent with the results of mRNA expression analysis. In addition, production of TGF-β2 showed the same trend as for mRNA expression, with higher production in FS than that in TS, although the differences were not significant. Among deep dermal fibroblasts, similar to results of mRNA expression analysis, FD showed lower production of TGF-β1 and CTGF than TD, and no clear trends were seen for type I collagen and TGF-β2 (Figure 4).

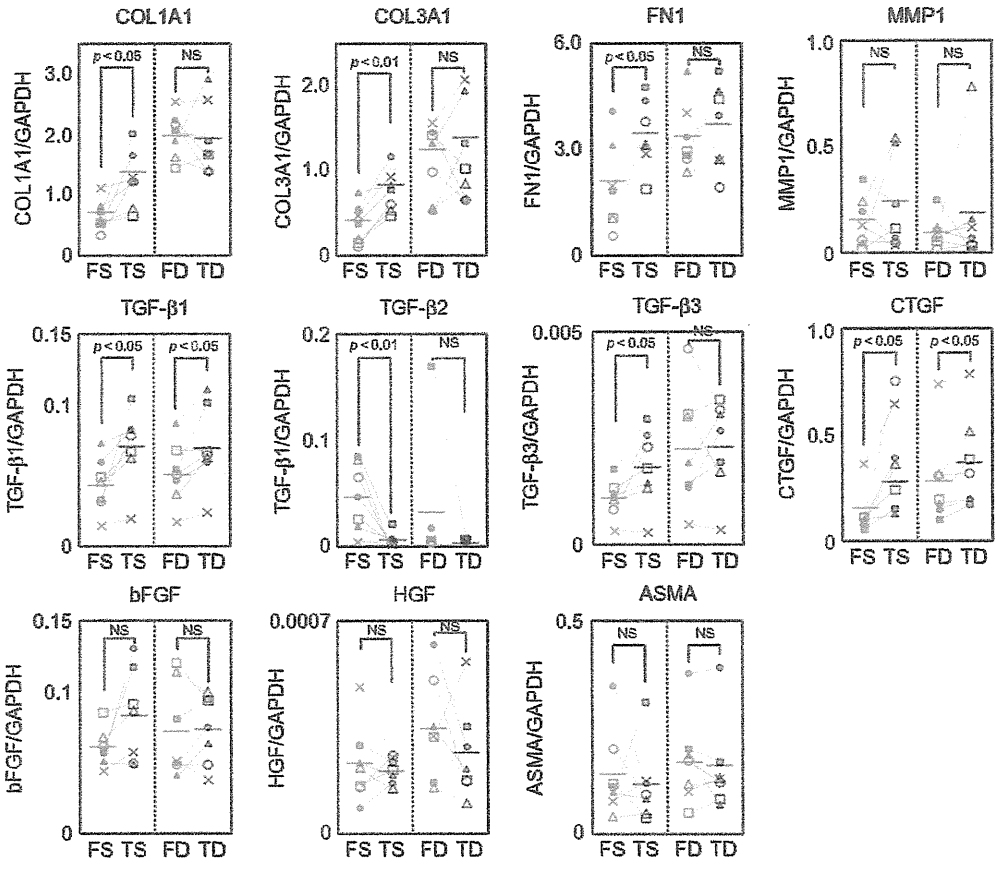

Figure 3. Expression of wound healing-associated factors by FS, TS, FD, and TD. mRNA expression of fibrosis-associated factors by FS, FD, TS, and TD ($n = 7$, each).

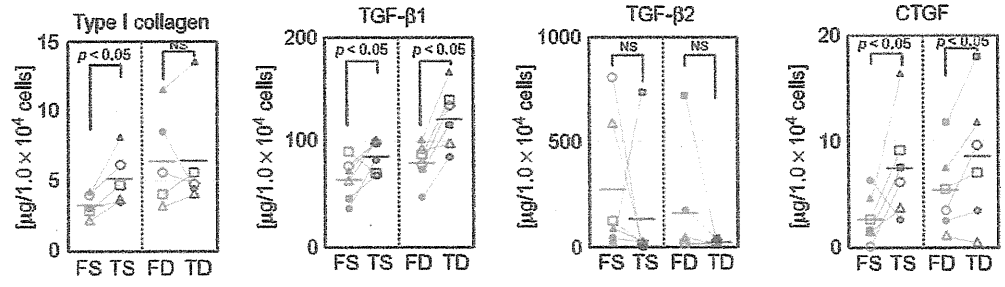

Figure 4. Production of wound healing-associated factors by FS, TS, FD, and TD. Production of type I collagen, TGF-β1 and TGF-β2, and CTGF by FS, FD, TS, and TD (for type I collagen, $n = 5$ for each; for others, $n = 6$ for each).

Discussion

In our analysis of seven paired FS, FD, TS, and TD samples from the same individuals, facial and trunk dermal fibroblasts obtained from the same layers of dermis showed identical morphology and proliferation kinetics, while differences in depth of origin distinctly affected cell morphology and proliferation kinetics, as indicated in previous reports [11–15]. On the other hand, the cellular density of facial and trunk dermal fibroblasts from the same depth of dermis in the same individuals showed significant, positive correlations. The proliferative capability of superficial and deep dermal fibroblasts is thought not to be influenced by anatomical site, but is specific to donor individuals.

In a subsequent study, mRNA expression of 11 genes considered to be associated with scarring (i.e., fibrosis formation) was investigated between facial and trunk dermal fibroblasts. Type I and III collagens, fibronectin, and collagenase expression were investigated because ECM production causes excess deposition of ECM, and were considered to be a profibrotic factor [8,9,26], while collagenase expression is considered to be an antifibrotic factor [11,27]. Other cytokines, such as TGF-βs, CTGF, bFGF, and HGF, were also investigated because these may be involved in fibrotic processes [11,27–31]. TGF-β1 and its downstream mediator CTGF are known to play particular important roles in hypertrophic scar formation and keloids [6,12,24,30,32] and are therefore considered to be dominant profibrotic factors. TGF-β2